*J. Fluid Mech.* (1990), *vol.* 221, *pp.* 613–639
*Printed in Great Britain*

# The transient settling of stable and flocculated dispersions

By FRANÇOIS M. AUZERAIS[1]†, R. JACKSON,[1] W. B. RUSSEL[1] AND W. F. MURPHY[2]

[1] Department of Chemical Engineering, Princeton University, Princeton, NJ 08544-5263, USA
[2] Schlumberger-Doll Research, Old Quarry Road, Ridgefield, CT 06877-4108, USA

(Received 18 January 1990)

An experimental investigation of the sedimentation of monodisperse colloidal silica spheres with grafted octadecyl chains with three different interaction potentials is presented. Small particles (0.27 μm) behaved as hard spheres in cyclohexane, but larger ones (0.60 and 0.94 μm) are weakly flocculated by van der Waals attractions. The smallest particles (0.08 μm) in hexadecane are strongly flocculated by attractions between the octadecyl layers. A medical computer tomography (CT) scanner provided an accurate and absolute density measurement without disrupting the process. For the hard spheres and the weakly flocculated systems, the kinetics of sedimentation for the dispersed phase could readily be predicted utilizing the flux curve. For flocculated networks, we found a power-law relationship between compressive yield stresses and solids fractions comparable with other experimental systems.

## 1. Introduction

Many industries must dispose of large volumes of slurries. In many instances the volumes of these effluents exceed the capacity of conventional methods of separation, such as centrifugation, pressure filtration, and oven drying. Separation is then restricted to processes in which gravity provides the driving force, such as batch settling. Kynch (1952) developed a mathematical treatment, predicting the formation of an incompressible sediment from monodisperse spheres with a known initial solids fraction and sedimentation velocity. To model sedimentation of colloidal particles, Davis & Russel (1989) incorporated a diffusion term into Kynch's equation. Although weak in comparison to convection throughout most of the suspension, diffusion can balance convection at volume fractions sufficiently near close packing. Buscall & White (1987) and Auzerais, Jackson & Russel (1988) constructed a complementary theory covering the full range of processes, from transient settling of large, stable particles to the slow consolidation of flocculated suspensions of submicron particles, and identified conditions for the existence of discontinuities in concentrations. Recently, Buscall (1990) has reviewed the current status of the theory.

The sedimentation of flocculated suspensions has been the subject of research for many decades, but controversy and confusion persist about the role of particle–particle interactions in settling and sediment consolidation. One reason is that

---

† Now at Schlumberger-Doll Research.

many natural dispersions are polydisperse with complex compositions which complicate the interactions between particles. Previous investigations (Michaels & Bolger 1962; Shannon *et al.* 1964; Been & Sills 1981; Fitch 1986; and Tiller & Yeh 1990) have helped to define the phenomena qualitatively but used poorly characterized heterodisperse material. Buscall (1981) examined the compression of flocculated suspensions above their gel point, showed that a small centrifugal acceleration rarely causes complete compaction of the solid phase. However, at equilibrium, concentration profiles provide information on the compressive yield stress of strongly flocculated dispersions. Barclay, Harrington & Ottewill (1972) applied a constant pressure to a small sample confined by a membrane within a compression cell to characterize the compressibility of flocculated suspensions. As the apparatus adjusts the liquid volume until equilibrium is obtained, the effect of the applied pressure can be measured. Increasing the pressure causes further compaction leading to a new equilibrium, and so on. This behaviour yields the yield stress as a function of equilibrium solids content.

Experiments to date have not distinguished between the period of decreasing settling rate in stable dispersions, associated with the region of slowing varying concentration above the sediment, and the effect produced by the consolidation of a compressible flocculated sediment. To do this requires detection of the relevant dependant variable, the density or the volume fraction, as a function of position and time, e.g. using an X-ray technique. The concept of deducing the density or concentration of solids from the attenuation of a beam of radiation is not new. Roscoe, Arthur & James (1963) described the early use of X-rays with lead-shot markers for obtaining shear and strain patterns within granular materials. In 1958, Gaudin & Fuerstenau measured local kaolin concentrations in settling beds as a function of time and position with X-ray adsorption techniques, giving careful consideration to the accuracy of the method. Later, Ondeyka, Henry & Verhoff (1978) monitored the sedimentation of mineral particles in opaque liquids at high temperatures and pressures by X-ray photography. However, this process is unsuitable for dynamic processes since the exposure time and X-ray intensity must be set to yield the maximum sensitivity in the relevant solids concentration range. Furthermore, stringent control on the processing of X-ray film and a high quality photo-densitometer are necessary to detect small changes in density. Been & Sills (1982) projected a collimated X-ray beam onto a soil sample and measured the transmission with a scintillation crystal and photomultiplier assembly which traversed the sample. Their work indicated the difficulties in applying radiation techniques to rapid settling and geometries with significant wall effects. Recently, Tiller & Yeh (1990) monitored batch settling of kaolin, as a function of distance and time, with a computerized axial tomographic scanner, pointing the way toward fast, accurate measurements. In parallel, other non-intrusive techniques have been developed with ultrasonic scanning appearing particularly convenient and promising (e.g. Howe & Robins 1990).

Computerized tomography (CT) is a new radiological imaging technique that measures density and atomic composition inside opaque objects. Despite a revolutionary advance in medical radiology since 1972, CT has only recently been applied in engineering. To understand the advantages of CT, let us first consider conventional X-ray radiography. The technique views an object from only one angle so that shadows from all irradiated matter along a ray path are superimposed and averaged, obscuring localized regions with small contrast. Two main limitations become obvious. First, it is impossible to display within the framework of a twodimensional X-ray picture all the information contained in the three-dimensional scene under view. Second, it is impossible to distinguish the separate densities of the individual substances through which the X-ray has passed. By comparison, CT scanners generate cross-sectional slices through the object by revolving an X-ray tube around the object and obtaining projections at many different angles. From a set of these projections, a cross-sectional image is reconstructed by algorithms (Payne & McCullough 1976). CT scanners have undergone considerable development since their creation. First-generation scanners used a single pencil-beam source and detector arrangement. Second-generation scanners improved image quality with multiple detectors in a translate/rotate configuration. A large improvement in speed occurred in the third-generation scanners, which rotate a fan-beam geometry with source and detectors distributed around the object. Finally, the fourth-generation scanners use a fan-beam geometry with a rotating source and a fixed ring of high-efficiency detectors. The second- to fourth-generation medical CT scanners are satisfactory for engineering applications because they have adequate X-ray energy and dose for scanning dense and complex material. Although the CT scanner was designed for medical purposes, we have successfully applied it to characterization of the sedimentation process.

## 2. Theoretical background

Kynch (1952) was apparently the first to formulate a theory for batch settling of identical particles accounting for the influence of gravity and hydrodynamic drag forces. He described the behaviour of the freely settling suspension by the conservation equation for the particles,

$$\frac{\partial\phi}{\partial t}+\frac{\partial[\phi U(\phi)]}{\partial\phi}\frac{\partial\phi}{\partial x}=0. \tag{1}$$

The solution to this partial differential equation depends on the form of the flux curve $\phi U(\phi)$ *vs.* $\phi$, with $x$ positive downward from an origin at the top of the liquid ($x = 0$). $U(\phi)$ denotes the local sedimentation velocity, assuming a dependence only on the local solids fraction $\phi$. The method of characteristics gives contours of constant $\phi$ with slopes given by

$$\frac{\partial x}{\mathrm{d}t}=\frac{\mathrm{d}[\phi U(\phi)]}{\mathrm{d}\phi}, \tag{2}$$

straight lines in the $(x,t)$ plane. Kynch assumed the sediment to be incompressible, i.e. with no flux and constant volume fraction.

Kynch found that, in certain circumstances, complete solutions exist only if the discontinuities, or shocks, are admitted. Despite the apparent simplicity of the case treated by Kynch, a variety of behaviour emerges depending on the shape of the flux curve and the initial spatial distribution of the particles. Rhee, Aris & Amundson (1986), summarizing the results of many earlier efforts, illustrate the method of characteristics for the usual shape of the flux curve $\phi U(\phi)$ by considering different uniform initial concentrations and identifying three different types of behaviour.

For a compressible sediment, the process depends on the contact forces transmitted between the particles. In order to introduce these forces, Auzerais *et al.* (1988) considered momentum balances for the liquid–solid system, including the stress $\sigma$

transmitted by interactions between solid particles. Neglecting inertial effects, the dimensionless momentum equation reduced to

$$u = U(\phi)\left[1-\frac{1}{(\rho-\rho_f)\,gL\phi}\frac{\partial\sigma}{\partial x}\right], \tag{3}$$

where $\rho$ and $\rho_f$ are the densities of the solid and the fluid, respectively, and $L$ is the natural lengthscale, the initial depth of the suspension. Then the dimensionless continuity equation becomes

$$\frac{\partial\phi}{\partial t}+\frac{\partial}{\partial x}\left[U(\phi)\left(\phi-\frac{1}{(\rho-\rho_f)\,gL}\frac{\partial\sigma}{\partial x}\right)\right] = 0. \tag{4}$$

If the stress transmitted between particles depends only on $\phi$, we can write $\sigma = \sigma(\phi)$ and, hence,

$$\frac{\partial\sigma}{\partial x} = \left(\frac{\mathrm{d}\sigma}{\mathrm{d}\phi}\right)\frac{\partial\phi}{\partial x}. \tag{5}$$

Then (4) and (5), together with the no-flux conditions at the top and bottom of the sedimentation column, constitute a complete description of the process.

To proceed further requires specific forms for the functions $U(\phi)$ and $\sigma(\phi)$. For stable dispersions, hard spheres provide a useful and realizable model for which simple, but robust constitutive relations for $U$ and $\sigma$ can be constructed from information in the literature. Experimental results reported by Buscall *et al.* (1982) for aqueous polystyrene latices and de Kruif, Jansen & Vrif (1987) for silica spheres in cyclohexane roughly follow the empirical equation

$$U(\phi) = (1-\phi)^{\mathrm{p}}, \tag{6}$$

with $5.5 \leqslant p \leqslant 6.6$. With $p = 6.55$, the sedimentation velocity conforms with the dilute limit derived by Batchelor (1972).

For stable dispersions of small particles the transmitted stress $\sigma(\phi)$ is equivalent to the osmotic pressure. The origin of this relationship can be illustrated by considering a dispersion with a monotonically varying volume fraction, e.g. decreasing upward. In the absence of an external field, such a spatially varying concentration represents a non-equilibrium state. Consequently, both particles and fluid molecules experience forces, proportional to the gradients in their respective chemical potentials (Batchelor 1976). Since the total force is zero and the chemical potential of the solvent is directly proportional to the osmotic pressure of a solute, or a colloidal particle, the thermodynamic force can be written for spheres of radius $a$ as

$$\frac{\mathrm{d}}{\mathrm{d}x}\sigma(\phi) = \frac{3kT}{4\pi a^3}\frac{\mathrm{d}}{\mathrm{d}\phi}[\phi Z(\phi)]\frac{\mathrm{d}\phi}{\mathrm{d}x}, \tag{7}$$

with $Z(\phi)$ known as the compressibility factor and $kT$ the thermal energy. In the dilute limit $Z(\phi) = 1+4\phi+O(\phi^2)$ (Thiele 1963) for hard spheres, and molecular dynamics simulations indicate that $Z(\phi)$ diverges as

$$Z(\phi) = \frac{1.85}{\phi_{\mathrm{m}}-\phi} \tag{8}$$

as $\phi \rightarrow 0.64$ (Woodcock 1981; Davis & Russel 1989).

To characterize the influence of interparticle forces, we define the Péclet number,

$$Pe = \tfrac{4}{3}\pi a^3 \frac{(\rho-\rho_f)\,gL}{kT} \tag{9}$$

which represents the ratio of the gravitational potential to the stress.

For flocculated dispersions neither the magnitude nor the functional form of the stress is known *a priori*. So one objective of the experiments was to test forms hypothesized in the literature or deduce the actual stress from the measured density profiles.

## 3. Experimental techniques

It has been known for almost a century that initially homogeneous suspensions of uniform particles do not sediment in a smooth, continuous fashion. Instead, layers of differing density develop with each layer appearing, to the eye, to be of nearly constant concentration. Measurement of solids concentration profiles without disrupting the process requires a sophisticated technique since light-absorption or light-scattering techniques are not applicable to opaque solutions. The present study also required higher spatial resolution and speed of measurement than most of the previous X-ray techniques. The ideal technique should have the following characteristics: a mono-energetic source of constant intensity, and energy at which the mass absorption coefficient does not vary with atomic number; a detector that measures radiation intensity accurately and quickly; and a geometrical configuration that preserves the relative position of the source, sample and detector while admitting to the detector only radiation that has passed through the sample. The present study employed Elscint's Exel 2002 BiModal CT, a second-generation scanner. A spectrum with a maximum voltage level of 140 kV provided optimum contrast and small fluctuations in attenuations. Generally an intensity of 42 mA and a continuous high voltage of 140 kV (corresponding to a peak of energy at 93 keV) were used.

### 3.1. *Calibration*

In the X-ray portion of the electromagnetic spectrum the photoelectric effect is the dominant absorption mechanism at energies well below 70 keV, and Compton scattering dominates above 70 keV where medical CT scanners normally operate. In photoelectric absorption, the total energy of the photon is transferred to an electron which is emitted from the atom of the absorbing material. In Compton scattering, the incident X-ray photon collides with atomic electrons, altering its trajectory and losing energy. This effect can be described as an elastic collision between a photon and a free electron initially at rest, altering the energy and/or the direction of the photons.

The energy dependence of the linear attenuation coefficient, $\mu$, is separated into two parts:

$$\mu = \mu_C + \mu_p, \tag{10}$$

where $\mu_C$ is the Klein–Nishina function for Compton scattering multiplied by the electron density, and $\mu_p$ represents the photoelectric absorption (Wellington & Vinegar 1987). The photoelectric and Compton contributions are expressed in the forms

$$\mu_p = a\frac{Z^m}{E^n}\rho, \tag{11}$$

$$\mu_C = b\rho, \tag{12}$$

where $Z$ is the atomic number, $E$ is the energy, $m$ and $n$ are constants in the range of 3.0 to 4.0, $\rho$ is the electron density (bulk density), and $a$ and $b$ are energy-dependent coefficients.

For our choice of operating conditions with the CT scanner, attenuations should behave according to (12). An empirical calibration obtained by plotting density or solids fraction against attenuation is nevertheless more accurate. CT attenuations are normally presented in an internationally standardized scale called Hounsfield units (CT#) (Hounsfield 1972) with air at −1000 and water at 0. With the Elscint Exel 2002, CT numbers range from −1000 to 3096. The CT# takes the form

$$\mathrm{CT\#} = 1000\frac{\mu_{\mathrm{m}}-\mu_{\mathrm{c}}}{\mu_{\mathrm{c}}} \tag{13}$$

where $\mu_{\mathrm{m}}$ is the measured attenuation of the sample and $\mu_{\mathrm{c}}$ is the attenuation of the calibration material (i.e. water). Any material suffices to zero the scale, but water lies conveniently in the middle of the range of densities used in our study. Then lighter/heavier materials than water have a negative/positive value of the CT#.

Calibration samples must be chosen carefully, with absorption similar to the solutions of interest and known uniform densities. Three different samples of silica particles of different sizes (0.60, 0.27, 0.08 μm) and known solid density were mixed in different proportions with cyclohexane or hexadecane. In addition, water, cyclohexane and hexadecane alone were scanned. Since we are operating in the Compton domain, the difference in atomic numbers between the solvents and the system composed of silica particles did not affect the measurement.

Each calibration specimen was in a 10 ml cylindrical container made of glass. Each tube rested on its side on the scanner bench in the middle of the scanning area, allowing cross-sections of the tube to be scanned. Uniformity of the density of each sample was confirmed. Then, all the attenuation measurements from the cross-section of the scanned tube yielded the average and standard deviation for the CT#. Figure 1 shows this calibration curve and its bounds for different samples of known bulk densities or solid fractions at 21 °C. The standard deviation for each measurement was ±6 CT#. The data fit a straight line which results in the calibration curve

$$\mathrm{CT\#} = -238.79+1210.43\,\phi. \tag{14}$$

## 3.2. *Experimental procedures*

Experiments were carried out in a 20 cm long tube for the transient settling or a 10 cm long tube for centrifugation. To avoid artifacts due to large density differences between the container and the suspension, a nylon tube of density 1.1 g/cm$^3$ was chosen. For our measurements, beam hardening occurs either when the density of the wall surrounding the sample exceeds considerably that of the sample, effectively absorbing all the photons, or when interfaces or sharp edges prevent detection of areas lying behind them. To eliminate sharp angles, the sample assembly has rounded inside and outside corners. The minimum wall thickness that we could reach without deformation of the tube was $\frac{1}{4}$ in. A cylindrical container was easier to tool but a square tube would serve the same purpose.

Before each settling experiment, the mass of dried silica particles was carefully measured in a preweighed 250 ml volumetric flask. The specific volume of solvent needed to give the desired suspension concentration was added to the flask with a calibrated burette. To homogenize the mixture, the silica was dispersed with a touchmixer or an ultrasonic bath. The dispersions in cyclohexane were maintained

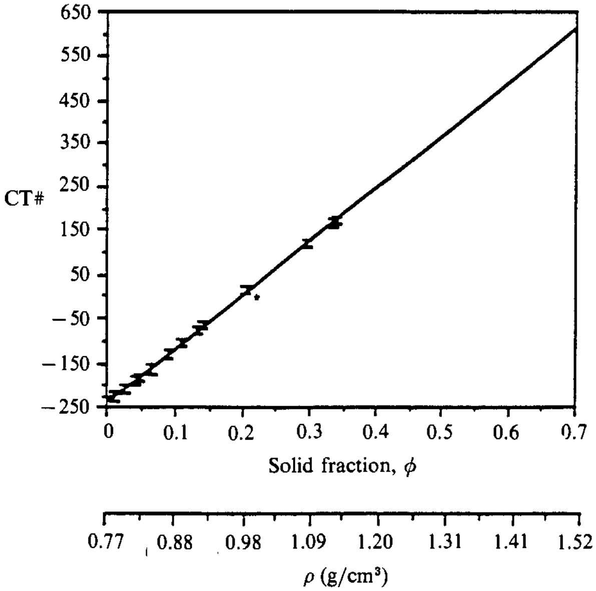

FIGURE 1. Calibration curve of CT# *vs.* bulk densities or solids fractions at 21 °C.

| $d_{\text{TEM}}$(μm) | $\phi_0$ | Initial height | Duration | Comments |
|---|---|---|---|---|
| 0.27 | 0.101 | 20.0 cm | 3 months | Transient settling in cyclohexane |
| 0.94 | 0.116 | 20.0 cm | 3 days | Transient settling in cyclohexane |
| 0.60 | 0.092 | 20.0 cm | 8 days | Transient settling in cyclohexane |
| 0.08 | 0.096 | 10.0 cm | 1 h | Centrifugation in hexadecane |

TABLE 1. Experiment details

at 21 °C in a cooling bath. For the hexadecane solvent, the suspension was mixed at 45 °C, well above the gel temperature. The specimen was then cooled to 21 °C in the nylon settling tube. With those initial temperature conditions, approximately half an hour elapsed before the centre of the tube reached the gel-point temperature (Carslaw & Jaeger 1959). The temperature in the scanner room was always maintained at 21 °C throughout each settling experiment. The scanner was calibrated daily with water and was tested with the unused solvent present in the sample to guarantee reproducibility between different measurements. Once a suspension was prepared, it was transferred to the settling column mounted vertically onto the scanning bench. Vertical alignment of the column was carefully checked before each experiment as even small inclinations would cause displaced solvent to flow preferentially up one wall of the column during settling. When proper vertical positioning of the scanned image was not achieved, we redispersed the sample to reestablish a uniform concentration at the initial time. Table 1 contains details of the samples and experiments referred to in this work.

### 3.3. *Performance*

The influence of the geometry of the container on the measurement had to be checked. To this end, the settling column was filled with deionized water and placed vertically on the bench of the scanner with the middle of the tube wall at the centre of the scanned area. A vertical cross-section along the tube was then scanned

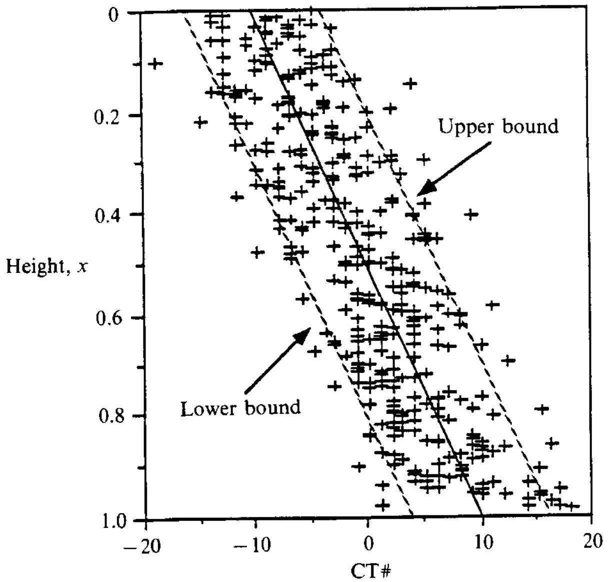

FIGURE 2. Influence of the geometry of the container on attenuation measurements for deionized water. $x$ is the dimensionless height.

producing the profile of the CT# in figure 2 with a reading of 0 at the centre of the tube ($x = 0.5$), as expected by the calibration, but an excess of + 10 CT at the bottom ($x = 1.0$) compensated by a deficit of 10 CT at the top ($x = 0$). To compensate for this systematic error, the correction

$$\mathrm{CT\#} = 10-20x \tag{15}$$

was added to every vertical profile. An estimate of the error in the measurement is provided by the scatter of the data. The upper and lower bounds on the measurements in figure 2 correspond to fluctuations of ±6 CT# about the mean shown by the solid line. These fluctuations, indicated also by the error bars representing the standard deviation of the calibration equation (14) plotted in figure 1, introduce a relative error of 2% in a measurement of the solid fraction. Greater precision is not required as the densities of the dried silica particles are only known to the third significant figure and fluctuations may arise owing to temperature variations. Experimental measurements described in §5 indicate a spatial resolution of the order of 2 mm.

## 4. Colloidal system

Colloidal dispersions consist of one or more materials finely dispersed in a fluid with the particle size normally between 10 and 1000 nm. One of the most important characteristics of a colloidal suspension is its stability (Derjaguin & Landau 1941; Verwey & Overbeek 1948). In stable suspensions the particles remain uniformly dispersed indefinitely in the absence of forces inducing sedimentation. On the other hand, the particle in unstable or flocculated suspensions form aggregates or flocs due to attractive forces.

From the large number of well-defined inorganic dispersions synthesized in recent decades (cf. Matijevic 1976), silica was chosen for three reasons: (i) the existence of a reliable and simple method due to Stöber, Fink & Bohn (1968) for preparing

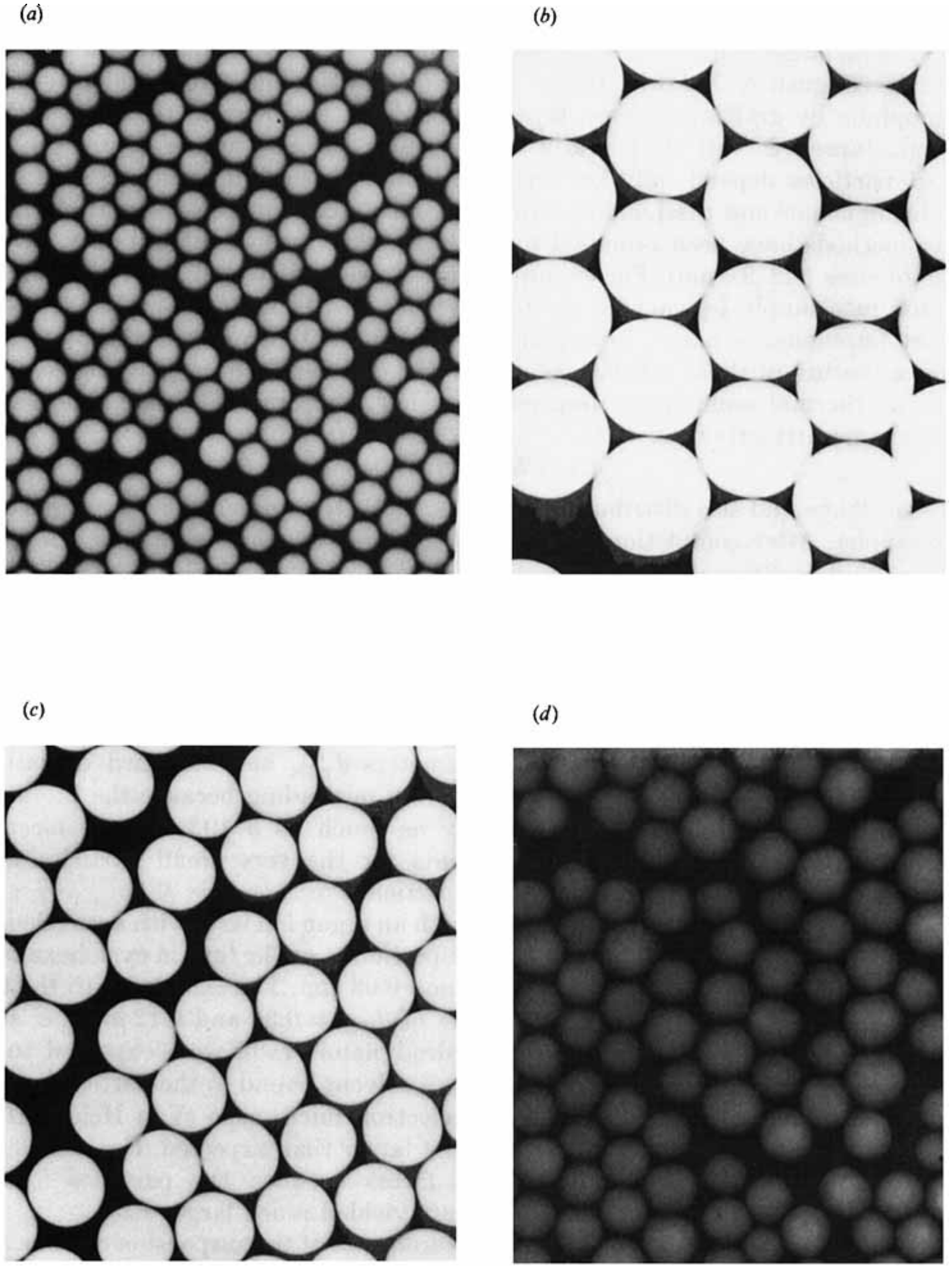

FIGURE 3. (*a*) Electron micrographs with $d_{\text{TEM}} = 0.27\ \mu\text{m}$ synthesized from a solution containing ethanol, 0.17 mol/l of TEOS, 1.2 mol/l of $NH_3$, and 3.2 mol/l of $H_2O$. Magnification = 19500. (*b*) Electron micrographs with $d_{\text{TEM}} = 0.94\ \mu\text{m}$ synthesized from a solution containing ethanol, 0.17 mol/l of TEOS, 2.0 mol/l of $NH_3$, and 5.5 mol/l of $H_2O$ and grown by one single addition of TEOS, 500 ml of $H_2O$ and 300 ml of EtOH. The final average diameter is 0.939 µm. Magnification = 19500. (*c*) Electron micrographs with $d_{\text{TEM}} = 0.60\ \mu\text{m}$ synthesized from a solution containing ethanol, 0.17 mol/l of TEOS, 2.6 mol/l of $NH_3$, and 7.14 mol/l of $H_2O$. Magnification = 19500. (*d*) Electron micrographs with $d_{\text{TEM}} = 0.08\ \mu\text{m}$ synthesized from a solution containing ethanol, 0.17 mol/l of TEOS, 0.8 mol/l of $NH_3$, and 2.2 mol/l of $H_2O$. Magnification = 90000.

spheres in the submicron size range with a narrow size distribution; (ii) the possibility of preparing larger spheres ($\geqslant 1$ μm) by controlled growth with the smaller particles as seeds (Bogush & Zukoski 1986); and (iii) the capability for rendering silica organophilic by grafting a dense layer of octadecyl chains onto the surface (Van Helden, Jansen & Vrij 1981). As a consequence, the interaction forces between coated particles depend only on the quality of the solvent with regard to the stabilizing chains and the London–van der Waals forces between the particle cores. Other methods have been proposed to produce uniform silica spheres over a wider range of sizes (0.2–2.0 μm). For example, Tan, Bowen & Epstein (1987) altered the reaction rate simply by varying the temperature ($-20$ to 60 °C) and the alcoholic solvent (methanol, ethanol, n-propanol, and n-butanol). However, the dangerous chemical nature of those solvents as well as the difficulties in keeping the reaction vessel at thermal equilibrium (especially at low temperature) made the growth process more attractive.

### 4.1. *Characterization*

The size, shape and size distribution of the particles were determined from electron micrographs. After completion of the coating process each sample was examined under a Phillips 400 transmission electron microscope by evaporating a drop of the suspension on a carbon-coated grid. Observation of the micrographs (figure 3) indicated a spherical shape for large particle sizes. The smaller particles have irregular shapes and greater polydispersity. Micrographs were converted to a corresponding digital image. Then, with the appropriate software, the total area covered by the particles was used to calculate the mean diameter. Calculations with over two hundred particles led to the diameters $d_{\mathrm{TEM}}$ and standard deviations presented table 2. However, these diameters are misleading because the literature indicates that the particles can shrink by as much as 5–10% in the electron microscope. Also, quantitative measurements for the very small particles were difficult because of the low contrast of the particles.

Dynamic light-scattering measurements with an argon ion laser with a wavelength $\lambda = 514.5$ nm were carried out with dilute dispersions ($\sim 1$ kg/m$^3$) in cyclohexane at 25 °C for particle sizes of $d_{\mathrm{TEM}} = 0.27$, 0.94, and 0.08 μm. The samples with the two smallest particles yielded average diameters of $d_{\mathrm{DLS}} = 0.36$ and 0.12 μm, i.e. sizes 30% larger than electron microscopy. Hydrodynamic radii were expected to be larger, since dynamic light scattering measures solvent bound to the particle surface and particles shrink under vacuum in the electron microscope (Van Helden *et al.* 1981), but the difference observed is somewhat larger than expected. For samples of the two largest particles van der Waals forces between the particles formed aggregates or flocs (§4.2) so the measurements yielded much larger sizes.

Particle densities were deduced from measurements of the suspension density as a function of solids mass fraction. Dry silica particles were weighed in a preweighed 50 ml flask. Cyclohexane was then added to the flask and the silica dispersed with a touch mixer. After allowing 24 h at 25 °C for trapped air to escape, cyclohexane was added again to the 50 ml mark and the flask reweighed. With the density of cyclohexane known, the particle density followed directly. This procedure was performed twice for each sample to verify the reproducibility of each measurement. The density ranged from 1.87 g/cm$^3$ for the largest size to 1.70 g/cm$^3$ for the smallest particle size, in line with the values reported by Van Helden *et al.* (1981).

| Average diameter (μm) | | |
|---|---|---|
| DLS | TEM | Density (g/cm$^3$) |
| 0.12 ± 0.01 | 0.08 ± 0.02 | 1.70 ± 0.03 |
| 0.36 ± 0.01 | 0.27 ± 0.03 | 1.80 ± 0.04 |
| | 0.60 ± 0.09 | 1.87 ± 0.04 |
| 1.34 ± 0.3 | 0.94 ± 0.09 | 1.77 ± 0.03 |

TABLE 2. Mean particle diameter and density measurements. (DLS and TEM refer to dynamic light scattering and transmission electron microscopy.)

### 4.2. *Choice of solvents*

Spherical silica particles of different sizes, densely covered with octadecyl chains allow interactions between the particles to be changed by varying the solvent (Jansen, de Kruif & Vrij 1986*a*, *b*). Interactions between two particles at separations of less than twice the thickness of the adsorbed layer require interpenetration or compression of the chains. In a good solvent such as cyclohexane the associated increase in the local hydrocarbon concentration in the gap produces an excess osmotic pressure and a repulsive force. The repulsion is very strong because the chains are short, uniform in length, and cover the surface densely. Indeed, the Utrecht group has shown that small silica particles (e.g. $d_{\mathrm{TEM}} = 0.27$ μm) dispersed in cyclohexane behave as hard spheres (de Kruif *et al.* 1985). The chains prefer to be surrounded by solvent molecules and there is essentially no repulsion until the adsorbed layers are in close proximity.

However, with an increase in particle size relative to adsorbed layer thickness (with $d_{\mathrm{TEM}} = 0.60$ and 0.94 μm), a London–van der Waals attraction gives a well-defined minimum in the interaction curve (Ottewill 1980). Mahanty & Ninham (1976) proposed constructing the potential $\Phi$ between equal spheres of radius $a$ at centre-to-centre separation $r$ as

$$\Phi = -\tfrac{1}{6}A_{\mathrm{eff}}(r-2a)\left(\frac{2a^2}{r^2-4a^2}+\frac{2a^2}{r^2}+\ln\frac{r^2-4a^2}{r^2}\right), \tag{16}$$

with the effective Hamaker constant, $A_{\mathrm{eff}}(r-2a)$, evaluated numerically for specific materials. To estimate the degree of flocculation of the systems with $d_{\mathrm{TEM}} = 0.60$ and 0.94 μm, we compute the Hamaker constant with a simplified approximation presented by Russel, Schowalter & Saville (1989), thereby sacrificing some accuracy but eliminating the numerical effort. For silica spheres bearing a thin layer of grafted octadecyl chains and dispersed in cyclohexane, the Hamaker constant varies from $A_{\mathrm{eff}}(0) = 3.96\times10^{-22}$ J at small separations to $A_{\mathrm{eff}}(\infty) = 2.66\times10^{-22}$ J for the fully retarded limit. The near-field limit determines whether the particles are flocculated. If the particles are strongly repulsed at a separation of about 4 nm, the magnitude of the dispersion energy follows at $0.8kT$ for a particle radius of 0.35 μm. Hence, our samples with particle diameters of the order of a micron should be weakly flocculated. As will be shown §5, settling experiments with $d_{\mathrm{TEM}} = 0.60$ or 0.94 μm apparently start with a suspension of flocs instead of a stable monodispersed silica system.

In a poor solvent, when the chains prefer to be surrounded by other chains, Jansen *et al.* (1986*a*, *b*) found that lowering the temperature of the dispersions caused strong attraction, i.e. a deep primary minimum in the potential. Their experiments on phase separation induced by temperature for different solvents suggested that the attraction upon cooling originates not with the van der Waals forces between the particle cores, but from the chains. For example, in hexadecane below 29 °C, silica particles less than 0.1 μm in diameter formed a gel which did not flow. Thus this system forms a volume-filling network which may then deform under normal gravity.

Next, we report measurements with the CT scanner of the settling behaviour of dispersions prepared with these silica particles.

## 5. Experimental observations

First, studies with initially uniform stable suspensions explore the region of slowly varying concentration above the sediment and the discontinuities bounding it. Second, experiments with larger particle sizes ($d_{\text{TEM}} = 0.94$ and $0.60\,\mu\text{m}$) illustrate deviations from the ideal case (Kynch) as the magnitude of the interparticle force increases and an intermediate shock develops. Third, a study with a flocculated suspension ($d_{\text{TEM}} = 0.08\,\mu\text{m}$) is designed to start with a space-filling network and examine the compressive response of a concentrated flocculated suspension above its gel point. We concentrate the particles toward closest packing in a low-speed centrifuge in experiments analogous to Buscall *et al.*'s (1982) and interpret the concentration profiles for different accelerations to determine a relation between stress and volume fraction.

Figures 4–7 (plates 1–4) show typical sets of CT-scan images with vertical and horizontal profiles of X-ray attenuation coefficients for the four different systems. In each case, the image of a vertical cross-section of the nylon container containing the dispersion is located at the centre of the layout. Three vertical concentration profiles taken along the tube at different radial positions are displayed at the right (these are essentially superimposed), and three horizontal concentration profiles taken transverse to the tube for different heights are at the left. The locations of these cuts are indicated by tick marks on the central photo. In the central image, the sedimentation column and its contents are shown in a grey scale which represents local X-ray attenuation. The brighter a pixel is, the larger the attenuation coefficient is (CT#), and, hence, the higher is the density. Darker regions indicate solvent-rich areas while lighter regions depict solids-rich areas. The image of the tube appears as a pair of vertical bars produced by the nylon wall. The nylon top and bottom of the tube are not shown.

The local X-ray attenuation coefficients can be obtained at any position within the tube. The plot is automatically scaled to give the smallest attenuation on the left and the largest one on the right with the range of attenuation displayed (only for vertical profiles) at the top. The three horizontal sections through the sedimentation column are not scaled but indicate relative attenuation change within the suspension. The deflections at each end of the horizontal plot arise from the difference in attenuation between the nylon wall and the suspension. If the densities were equal, no change in attenuation would be seen. When the suspension becomes denser/lighter than the wall, its display lies above/below the nylon readings. Horizontal plots should detect any effects due to channelling or the walls. To illustrate different settling behaviour, each individual case is now discussed.

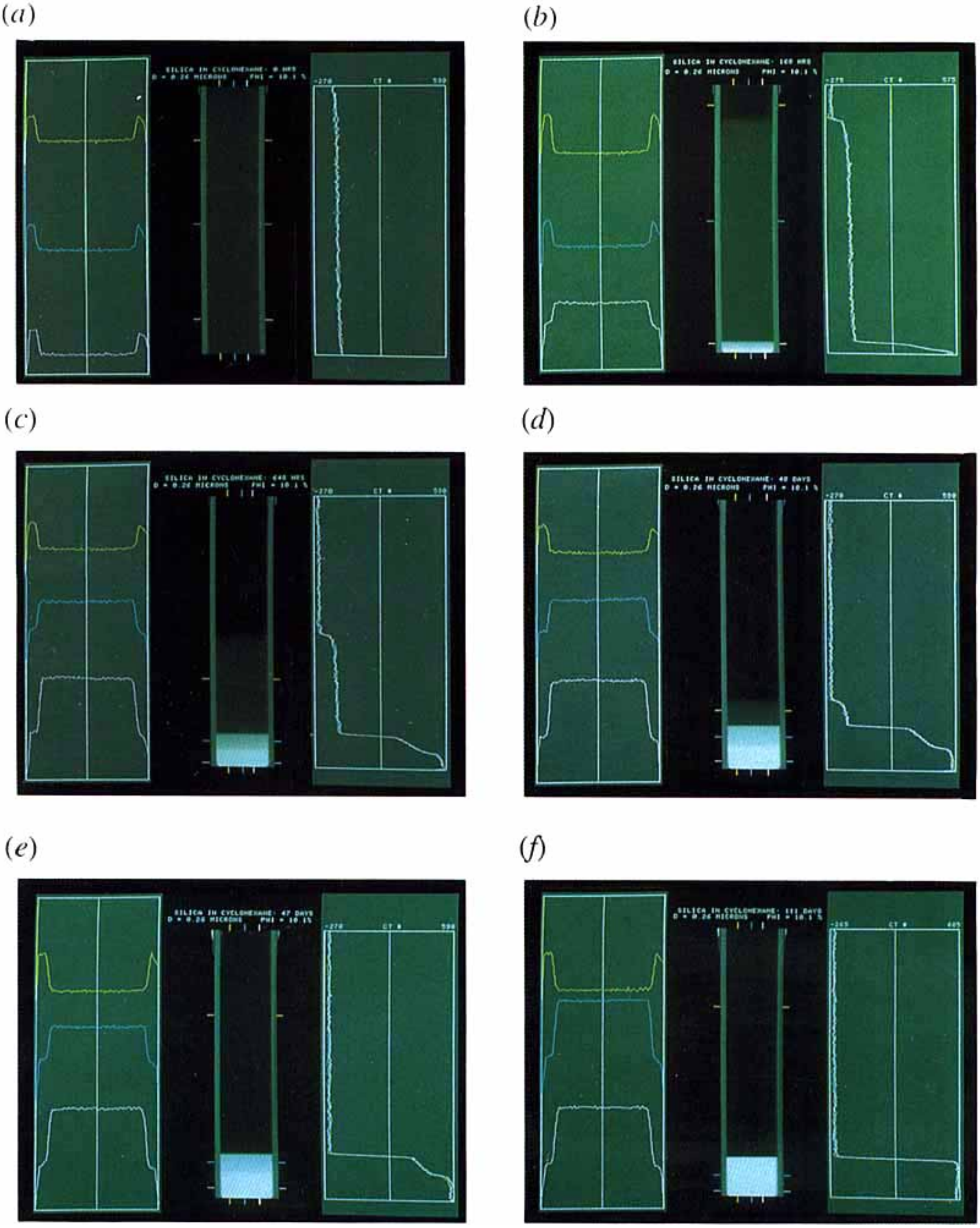

FIGURE 4. CT-scan images with vertical and horizontal profiles of X-ray attenuation coefficients at (*a*) 0, (*b*) 168 h, (*c*) 648 h, (*d*) 40 days, (*e*) 47 days, and (*f*) 111 days for $d_{\mathrm{TEM}}=0.27$ μm in cyclohexane.

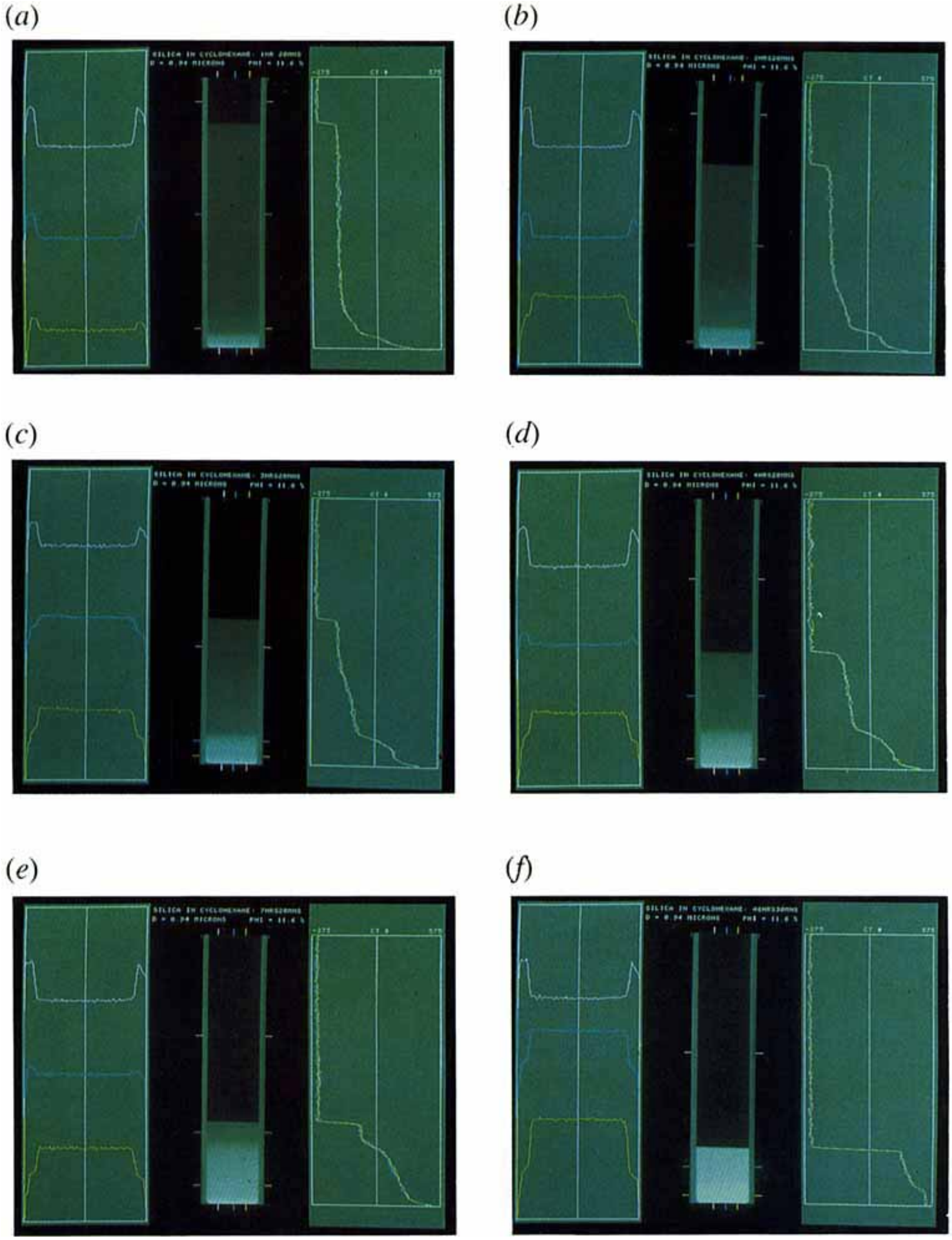

FIGURE 5. CT-scan images with vertical and horizontal profiles of X-ray attenuation coefficients at (*a*) 80 min, (*b*) 140 min, (*c*) 200 min, (*d*) 260 min, (*e*) 440 min, and (*f*) 2790 min for $d_{\mathrm{TEM}} = 0.94\ \mu\mathrm{m}$ in cyclohexane.

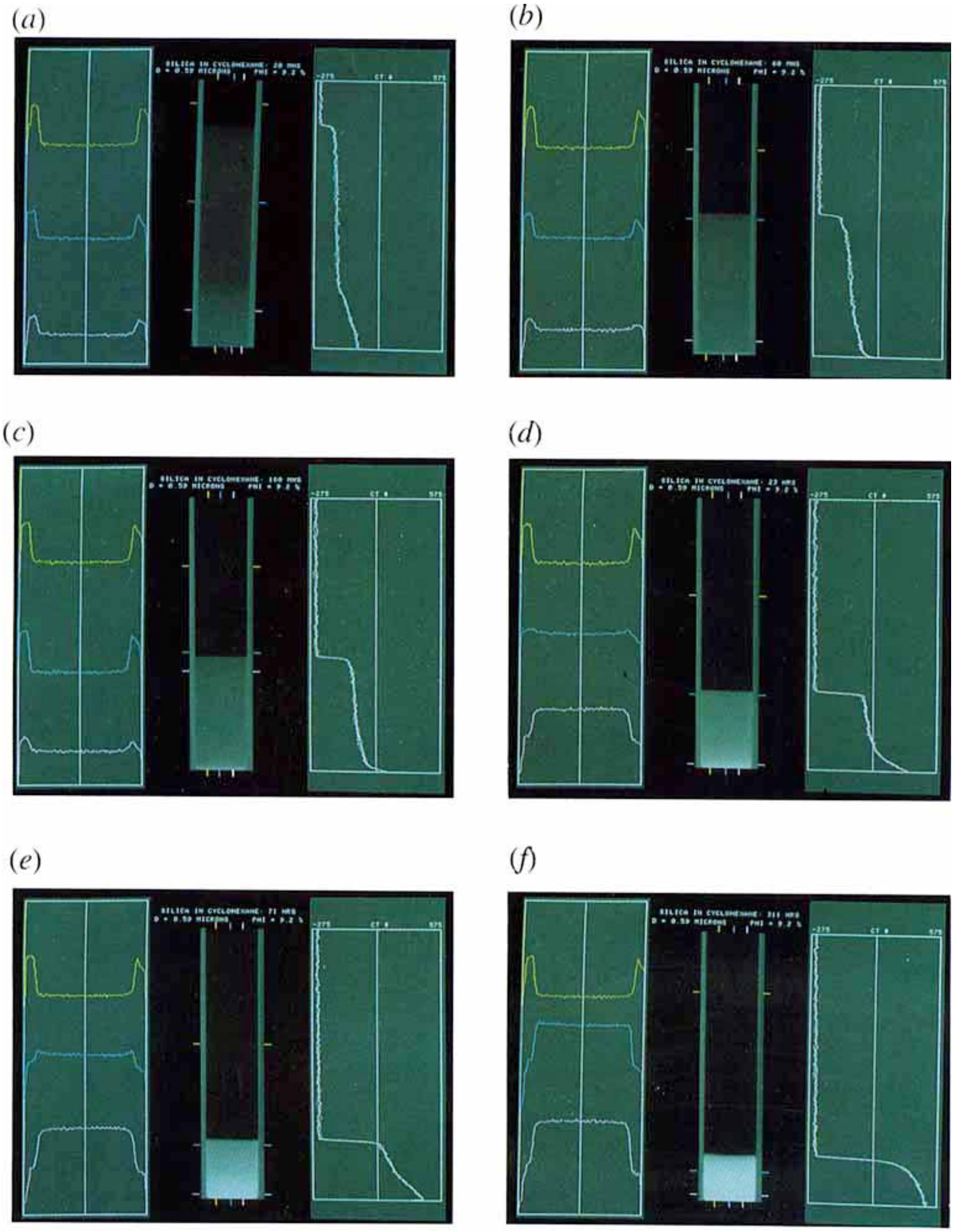

FIGURE 6. CT-scan images with vertical and horizontal profiles of X-ray attenuation coefficients at (*a*) 20 min, (*b*) 60 min, (*c*) 180 min, (*d*) 23 h, (*e*) 71 h, and (*f*) 311 h for $d_{\mathrm{TEM}}$=0.60 $\mu$m in cyclohexane.

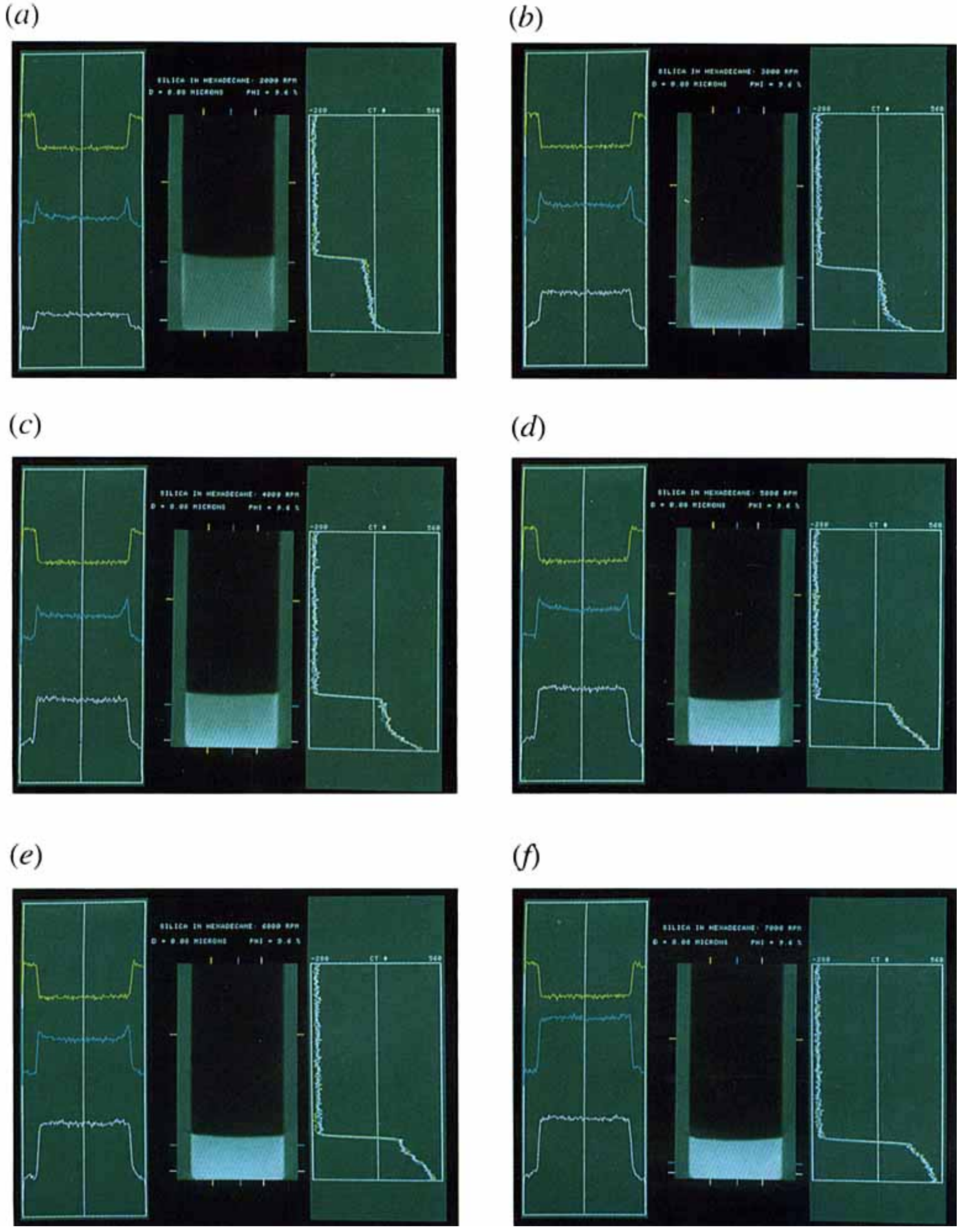

FIGURE 7. CT-scan images with vertical and horizontal profiles of X-ray attenuation coefficients at centrifugal accelerations (*a*) 2000 r.p.m. (*b*) 3000 r.p.m. (*c*) 4000 r.p.m. (*d*) 5000 r.p.m. (*e*) 6000 r.p.m. (*f*) 7000 r.p.m. for $d_{\mathrm{TEM}} = 0.08$ μm in hexadecane.

### 5.1. *Hard spheres* ($d_{\mathrm{TEM}} = 0.27$ *μm*) *in cyclohexane under normal gravity*

The transient settling of a suspension of spherical monodispersed silica particles ($d_{\mathrm{TEM}} = 0.27$ μm) in cyclohexane is examined first. Figure 4 (plate 1) shows a sequence of CT-scan images at six different times: (*a*) 0 h, (*b*) 168 h, (*c*) 648 h, (*d*) 40 days, (*e*) 47 days, (*f*) 111 days. The suspension is initially homogeneous with $\phi_0 = 0.101$ as indicated in figure 4(*a*) by flat profiles at each level. This initial state, before the particles settle significantly, quantifies the effects due to the density difference between the suspension and the wall, indicating that any sharp change in density cannot be resolved spatially to better than four pixels or 2 mm.

The images in figure 4(*b*–*d*) highlight four different regions within the suspension. The dark region at the top corresponds to the supernatant fluid. Next comes a zone of uniform attenuation consisting of the initial suspension. This contrasts sharply with a bright intermediate region just below it. The still brighter fourth region at the bottom represents the sediment. Figure 4(*e*) emphasizes the final stage of the settling, with only three regions remaining and a major change in attenuation between the supernatant zone and the denser region underneath. Ultimately the process reaches equilibrium (figure 4f) with a discontinuity remaining between the consolidated sediment and the solvent above it. Measurements with four neighbouring pixels confirm our earlier statement on spatial resolution. For each settling region and the sediment, horizontal plots depict no change in density within the suspension from either wall effects or channelling.

By observing the variation of attenuation with time, one is able to monitor the dynamic behaviour of the sedimentation process. Figure 9 (§6) collects vertical concentration profiles at 8, 15, 22, 29, 36, 43, 56, and 111 days (broken lines). Converting the local X-ray attenuation coefficients, which range from −275 to 575 CT#, into solid fractions using equations (14) and (15), clearly distinguishes the four regions. Also two distinct interfaces are visible on this plot the supernatant–suspension interface in the upper part and a discontinuity between the initial suspension and a zone of gradually increasing concentration in the lower part of the cylinder (just above the sediment). As time evolves, the supernatant–suspension interface descends to meet the rising sediment, completing the process after 111 days to give a maximum packing of about 0.67. The main features of the plot are similar to the numerical example treated in the theory (Auzerais *et al.* 1988) with stable suspensions.

### 5.2. *Settling of weakly flocculated suspensions*

#### 5.2.1. *Aggregated* 0.94 *μm particles in cyclohexane under normal gravity*

We next examine the settling of a suspension of 0.94 μm monodispersed silica spheres in cyclohexane. Figure 5 (plate 2) summarizes a series of CT scan images at times (*a*) 80 min, (*b*) 140 min, (*c*) 200 min, (*d*) 260 min, (*e*) 440 min, and (*f*) 2790 min. The homogeneous suspension of initial solid fraction $\phi_0 = 0.116$ is not presented here but has the same features as the previous case. Five distinct regions appear in the images in figure 5(*a*–*c*). At the top of the tube, a dark region represents the pure solvent with the lowest attenuation (−240 CT#). Beneath the supernatant, the attenuation jumps to a constant value, indicating a sharp interface with the initial suspension. A zone of moderate increase in concentration follows, separated by a discontinuity from a bright zone showing a gradient in concentration. A concentrated zone near the base of the sediment begins as a very thin layer after about three hours but grows to (figure 5*d*) a distinctly white region with $\phi \sim 0.60$. After four hours (figure 5*d*), the zone of uniform concentration disappears into the region of smoothly varying volume fraction which is separated from the more concentrated suspension below by a weak discontinuity. Figure 5(*e*) illustrates the very slow build-up of the sediment. Figure 5(*f*) depicts the final phase of the process, where the supernatant–suspension interface descends while the suspension–sediment interface moves upward to eventually merge and form a sharp single interface. The attenuation coefficients in the sediment are constant, indicating $\phi \sim 0.63$.

Figure 12 (§6) collects the profiles at the various times 1, 2, 3, 4, 5, 7, 11, 23, 46, 95 h and finally 7 days (broken lines). The five regions can be identified clearly. The primary distinguishing characteristic of this settling behaviour lies in the rapid change in concentration for $0.23 \leqslant \Phi \leqslant 0.4$. Finally, horizontal cross-sections within the sample showed a flat profile of attenuations, so no wall effects were observed.

### 5.2.2. *Aggregated* 0.60 μ*m particles in cyclohexane under normal gravity*

We now investigate the settling of a suspension of 0.60 μm monodispersed silica spheres in cyclohexane. Figure 6 (plate 3) reflects a series of CT scans at (*a*) 20 min, (*b*) 60 min, (*c*) 180 min, (*d*) 23 h, (*e*) 71 h, and (*f*) 311 h for $\phi_0 = 0.092$. For the first 60 min of the sedimentation experiment, only three distinct regions appear. The interface between the solvent and the zone of initial concentration is sharp and the top of the suspension remains at its initial density as it settles. A region about $\phi = 0.20$ rises from the bottom (figure 6*a*, *b*). After two to three hours (figure 6*c*), the initial suspension and the settled particles beneath meet and the process slows considerably. Only after 20 h does a relatively dense bed of particles appear at the base of the column (figure 6*d*, *e*) with a maximum packing of about $\phi = 0.60$. This white sediment grows and finally meets the supernatant interface, establishing equilibrium after 300 h. Despite a smaller particle size relative to the sample F18, the time to reach full consolidation is much shorter for approximately the same initial concentration.

Certain aspects of the settling behaviour of this sample plotted in figure 14 (§6) (broken lines) result from weak flocculation. At low solids content, flocs may settle faster than individual particles. But after 3 h, when the individual flocs pack together to form a network structure, i.e. one large floc, a region of higher concentration with $\phi = 0.25$, the sedimentation rate is considerably decreased by the stresses transmitted through the particle contacts. This disordered sediment gradually consolidates but cannot reach maximum packing because of the forces preserving the open structure of the flocs. Increasing the gravitational force would allow further compaction. For this sample, no wall effects were noticeable from the horizontal plots.

### 5.3. *Strongly flocculated network in hexadecane under centrifugal acceleration*

Centrifuge experiments illustrated schematically in figure 8 involve the following procedure. An initially homogeneous dispersion of silica particles in hexadecane with $\phi_0 = 0.096$ ($d_{\mathrm{TEM}} = 0.08$ μm) is poured into a centrifuge tube to a height $L$ and permitted to cool to room temperature and thereby form a volume-filling gel. The sample is spun at a particular speed until an equilibrium height is established and then removed from the centrifuge for scanning. After measurement of the concentration profile, the tube is reinstalled in the centrifuge and the speed increased. The exercise is repeated at centrifugation speeds ranging from 1500 to 7000 r.p.m. The temperature of the centrifuge was set at 21 °C but fluctuated about 2 °C during the initial phase of the process. The experiment was repeated to test

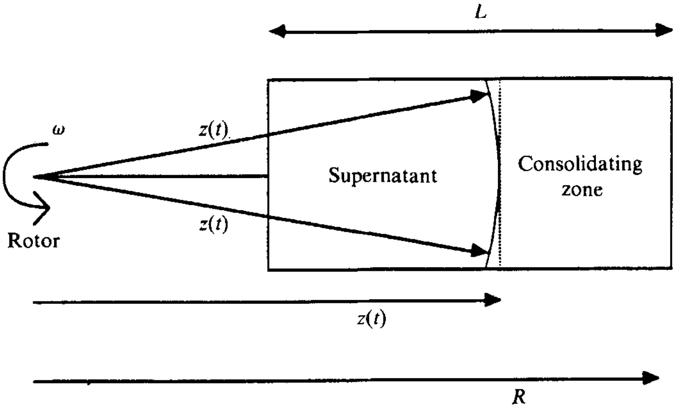

FIGURE 8. Schematic illustration of the centrifuge experiments.

reproducibility. Under normal gravity no settling is noticeable on the timescale of these experiments.

Figure 7 (plate 4) illustrates the effect of centrifugal acceleration at r.p.m. values of (*a*) 2000, (b) 3000, (*c*) 4000, (*d*) 5000, (*e*) 6000, and (*f*) 7000 on the network or gel. The six images reveal a very clear interface between the pure solvent (dark area) and the sediment beneath. The curvature of this interface indicates the non-uniformity of the centrifugal forces across the sedimentation column. Figure 8 shows the difference between the locus of points at a distance $z(t)$ corresponding to a uniform force field (broken line) and the radial centrifugal forces emanating from the rotor (full line at a radius $x(t)$). These radial forces also explain the predominant vertical lines on each wall, best seen in figure 7 (a, b). Quantitatively, a ratio of $\frac{1}{8}$ between the radius and the height $R$ of the sediment (figure 8) corresponds at the base of the sediment to an 8% increase in the centrifugal force from the centre of the settling column to the wall. Horizontal concentration profiles within the dispersion exhibit this effect but wall effects remain unimportant.

As already observed by Buscall (1981), increasing the acceleration never totally consolidates the solid phase. Rather, a definite equilibrium sediment volume is attained. The plots for different rotor speeds show the initial network yielding throughout with no zone at the initial volume fraction. The upper surface of the suspension appears as sharp as our spatial resolution allows and, below the interface, the solids concentration increases monotonically with depth.

Having observed a variety of settling behaviour, we seek solutions to the equations of motion, using an appropriate combination of Kynch theory, shock conditions and numerical integration techniques, to predict the rate of fall of the suspension surface, the rate of rise of the sediment surface, and the solids concentration profiles within both the settling suspension and the compacting sediment. These will be compared with the results of the experimental measurements described above.

## 6. Comparison of the theory and experimental results

### 6.1. *The hard-sphere case*

An empirical equation for the settling velocity of the form

$$U(\phi) = (1-\phi)^{(\alpha-\beta\phi)}, \tag{17}$$

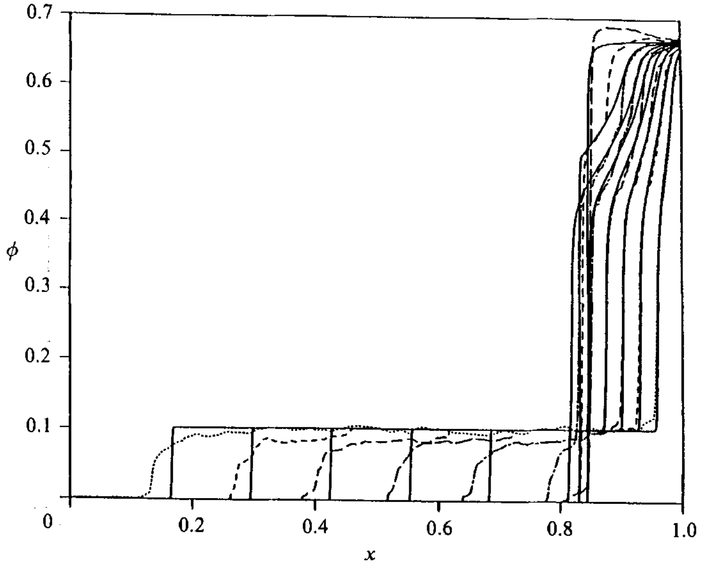

FIGURE 9. Concentration profiles at various times (8, 15, 22, 29, 36, 43, 56, and 111 days) for $\phi_0 = 0.101$ and $Pe = 1.5 \times 10^4$ for stable suspension in cyclohexane ($d_{\text{TEM}} = 0.27$ µm). Comparison between the experimental data (broken lines) and the theoretical profiles (full lines).

with the constants $\alpha = 6.55$ and $\beta = 1.57$ conforms to the limit found by Batchelor (1972) for $\phi \rightarrow 0$, and the exponent of 5.5 extracted by Buscall (1981) from data for a concentrated suspension of stable latices. From our settling measurements, we estimate a solids volume fraction at maximum packing of $\phi_m = 0.67$. This exceeds random close packing, probably indicating some degree of crystallization as reported by Davis, Russel & Glantschnig (1989). Equation (17) is scaled by $v_t$, the terminal settling velocity of an isolated particle in an infinite body of fluid,

$$v_t = \frac{2}{9}\frac{a^2(\rho - \rho_f)g}{\mu} \tag{18}$$

with $a$ the radius of the particle and $\mu$ the viscosity of the fluid. For a mean radius of $a_{\text{DLS}} = 0.185$ µm, the Stokes' velocity of 80 nm/s yields at Péclet number of $1.5 \times 10^4$ for a cylinder of height 0.2 m. To solve (4) numerically for this case also requires the osmotic pressure (8) for hard spheres. Figure 9 compares the experimental data (broken lines) and the theoretical profiles (full lines) obtained at 8, 15, 22, 29, 36, 43, 56, and 111 days.

The variation of $\phi$ during the settling process follows from the geometry of the flux curve in figure 10. The sedimentation curve, scaled by $v_t$, has one concave region. From an initial solids fraction $\phi_0 = 0.101$, direct contact between the suspension and the sediment is not possible. However, as shown in Auzerais *et al.* (1988), we can construct a compression shock tangent to the sedimentation curve at $\phi_t = 0.42$. Then, a falling rate period follows with $\phi$ gradually increasing in the interval $[\phi_t, \phi_b]$, until the material can contact the rising sediment surface.

The transition from the uniform suspension at $\phi = 0.10$ to the falling rate region with $\phi = 0.42$ and the concentration gradients within the falling rate period closely resemble those computed, indicating that the constitutive equations represent the process. However, the solution within the sediment, leading to $\phi_m = 0.67$, does not

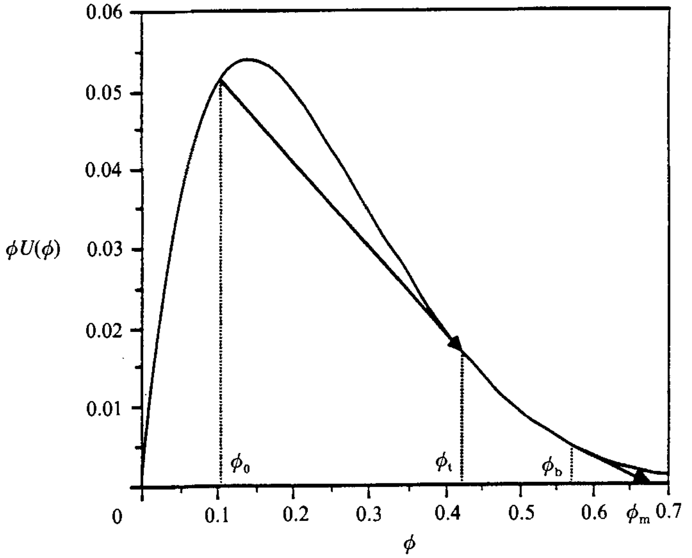

FIGURE 10. Schematic illustration of a flux curve with associated discontinuities for $d_{\text{TEM}} = 0.27$ μm.

compare well with the theory. In fact, the discontinuity observed represents a transition from a disordered phase of solid fraction $\phi = 0.56$ to an ordered structure with $\phi = 0.67$ which is not incorporated into the theory, but will be discussed in §6.4.

The very diffuse interface measured between the supernatant and the initial uniform concentration at the top of the column also differs from the theoretical predictions and is not accounted for by the small polydispersity of the particles (standard deviation = 25 nm). Nor does diffusion explain the effect since particles (with $D_0 = kT/6\pi\mu a \approx 1.1 \times 10^{-12}$ $\text{m}^2/\text{s}$) only diffuse abut $(D_0 t)^{\frac{1}{2}} \approx 300$ μm/day or a dimensionless distance of $10^{-2}$ in 7 days. However, realistic justification can be found in the design of the settling tube. The top of the tube was partially cut away on one side to trap any air bubbles and avoid a gap between the nylon top and the suspension. Consequently, particles initially in the fluid within this cutout, away from the X-ray beam, lag particles in the main part of the tube, producing a small concentration gradient which persists owing to the timescale of the experiment.

Despite the minor differences between the real behaviour and the theoretical concentration profiles just described, the model successfully predicts sedimentation behaviour of this stable suspension and manifests clearly the limiting nature of the Kynch solution.

### 6.2. *Weakly flocculated suspensions in cyclohexane*

Although sedimentation of silica particles of small diameter ($< 0.1$ μm) in cyclohexane has been widely studied (Jansen *et al.* 1986*a*, *b* and Kops-Wekhoven & Fijnaut 1981), little is known about the behaviour of larger silica particles. As will be seen, dispersion forces between the particle cores create weakly flocculated systems which settle quite differently from the previous example.

We could not measure the interparticle forces directly but have characterized in detail the flux/concentration relationship by tracking the supernatant–suspension interface for a range of initial volume fractions. These sedimentation experiments were performed with particles of $d_{\text{TEM}} = 0.60$ and 0.94 μm dispersed in cyclohexane

| $d_{\text{TEM}} = 0.94\ \mu\text{m}$ | | $d_{\text{TEM}} = 0.60\ \mu\text{m}$ | |
|---|---|---|---|
| $\phi$ | $U(\phi)$ [μm/s] | $\phi$ | $U(\phi)$ [μm/s] |
| 0.028 | 1.11 | 0.062 | 0.627 |
| 0.042 | 0.901 | 0.093 | 0.367 |
| 0.070 | 0.571 | 0.124 | 0.196 |
| 0.116 | 0.265 | 0.155 | 0.091 |
| 0.140 | 0.203 | 0.185 | 0.049 |
| 0.162 | 0.151 | 0.216 | 0.008 |
| 0.189 | 0.100 | 0.247 | 0.005 |
| 0.216 | 0.080 | 0.309 | 0.001 |
| 0.243 | 0.070 | | |
| 0.270 | 0.067 | | |
| 0.350 | 0.029 | | |

TABLE 3. Sedimentation velocities

at different initial solids fractions in vertical 10 ml graduated cylindrical Pyrex tubes about 0.12 m high and with an internal diameter of 10 mm in a controlled temperature bath at 21 °C. After the tube and its contents had equilibrated thermally, the suspension was agitated with a touchmixer and the tube was set vertical. The height of the interface at the top of the suspension was measured with a cathetometer at different times and velocities calculated by linear regression to obtain the results in table 3.

The dimensionless sedimentation velocity for the particles with $d_{\text{TEM}} = 0.94\ \mu\text{m}$ follows the empirical formula

$$\left.\begin{aligned} U(\phi) &= 94.17(1-14.78\phi+99.76\phi^2-377.52\phi^3+784.81\phi^4) && \text{for}\, \phi \leqslant 0.35, \\ U(\phi) &= 94.17(1-\phi)^{10.72} && \text{for}\, \phi > 0.35, \end{aligned}\right\} \tag{19}$$

with the velocity scaled by $v_t = 4.8 \times 10^{-7}$ m/s, computed from (18) with $d_{\text{TEM}}$. The apparent terminal velocity, $v_t = 4.5 \times 10^{-5}$ m/s estimated by extrapolating the measured velocities to infinite dilution, corresponds to an equivalent radius of 4.5 μm, (18). The order-of-magnitude difference in the particle size indicates the degree of flocculation of the initial dispersion. Thus settling apparently starts with an homogeneous suspension of large flocs.

In the case of $d_{\text{TEM}} = 0.60\ \mu\text{m}$, the best fit of the experimental data gives

$$\left.\begin{aligned} U(\phi) &= 752.38(1-13.59\phi+62.89\phi^2-98.582\phi^3) && \text{for}\, \phi \leqslant 0.19, \\ U(\phi) &= 752.38(1-\phi)^{(25-20\phi)} && \text{for}\, \phi > 0.19, \end{aligned}\right\} \tag{20}$$

which is scaled by $v_t = 2.1 \times 10^{-7}$ m/s computed from (18). The apparent terminal velocity at infinite dilution, $v_t = 1.6 \times 10^{-4}$ m/s, gives an equivalent radius of 8.2 μm, almost thirty times the TEM measurement, again suggesting a suspension of large flocs.

For both samples, difficulties in preparing samples of initial solid fraction greater than 0.4 necessitates extrapolation of the data to obtain the requisite constitutive equations. Hence the empirical equation $(1-\phi)^p$ was chosen with an exponent $p$ to give a velocity at maximum packing equivalent to the hard-sphere limit and adjusted somewhat to reproduce the slopes of characteristics (contours of constant $\phi$ given by (2)) within the sediment.

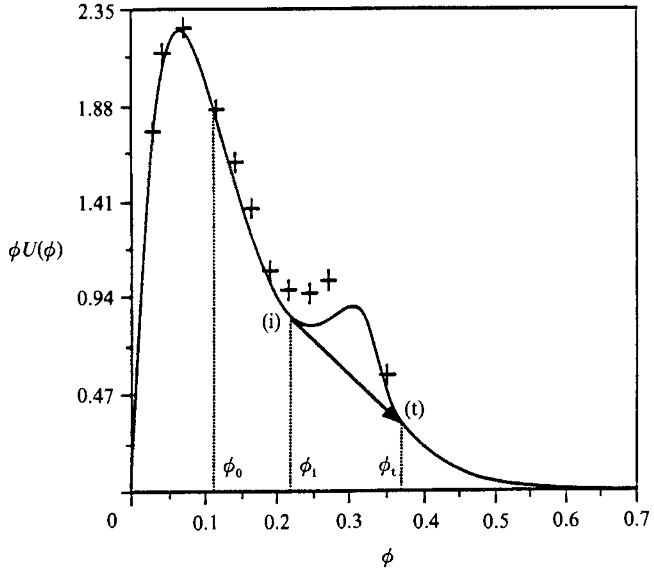

FIGURE 11. Schematic illustration of a flux curve with associated discontinuities for $d_{\text{TEM}} = 0.94\ \mu\text{m}$.

The corresponding expression for the stress is more difficult to assess since these systems lie between stable dispersions, for which the osmotic pressure is appropriate and reasonably well characterized, and strongly flocculated dispersions, for which the compressive yield stress is relevant. For the present, we merely adopt the functional form of (8) and treat the Péclet number as an adjustable parameter.

### 6.2.1. *Numerical comparison for $d_{\text{TEM}} = 0.94\ \mu m$ in cyclohexane*

Figure 11 shows the experimental values of the solids flux as a function of the solids fraction for $d_{\text{TEM}} = 0.94\ \mu\text{m}$ with the full line derived from (19). The sedimentation curve is found to be doubly concave. Kynch (1952) briefly discussed such a possibility and Shannon, Stroupe & Tory (1963) found the flux plot for rigid spheres in water to be doubly concave. Previously, Tory (1961), studying the batch settling of $CaCO_3$ in water, found a flux curve with two markedly concave regions based on initial batch settling rates and cited additional evidence from the literature.

From this flux curve and the stress from (8) with $Pe = 10^3$ (rather than $2 \times 10^5$ as expected from (9)), the batch settling profiles in figure 12 may be predicted. Starting with $\phi_0 = 0.116$, the double concavity in the sedimentation curve does not allow direct contact between the initial concentration and the sediment. Instead, a concentration gradient develops and propagates until the volume fraction reaches point (i) on the curve corresponding to $\phi_i = 0.22$. Then a compression shock (represented by an arrow, figure 11) can be constructed tangent to the flux curve at a point (t) with $\phi_t = 0.37$. A falling rate period follows with $\phi$ continually increasing to meet the rising sediment surface.

Figure 12 compares the experimental data (broken lines) and the theoretical profiles (full lines) hourly to 5 h, then at 7, 11, 23, 46, 95 h and finally 7 days where the sediment is totally consolidated. From 1 to 7 h, the two falling rate periods resemble qualitatively those predicted by the theory. The two regions are separated by an intermediate jump as anticipated from the form of the flux curve. The theory

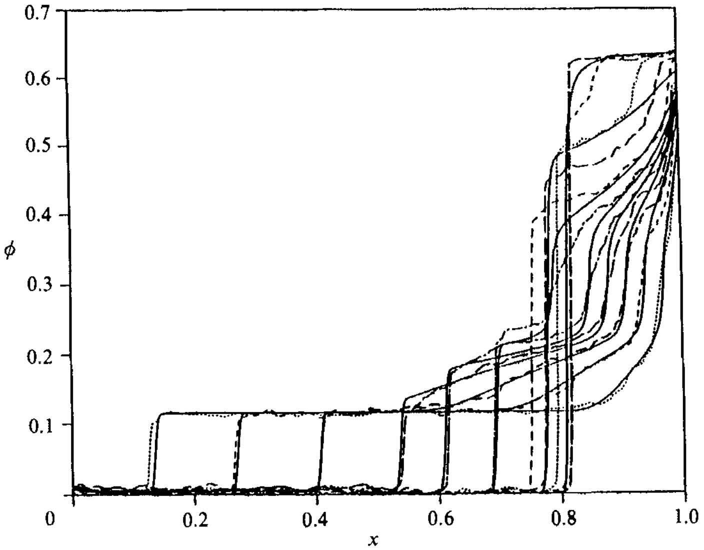

FIGURE 12. Concentration profiles at various times (1, 2, 3, 4, 5, 7, 11, 23 ,46, 95 h, and 7 days) for $\phi_0 = 0.116$ and $Pe = 1000$ for weakly flocculated suspension in cyclohexane ($d_{\mathrm{TEM}} = 0.94$ µm). Comparison between the experimental data (broken lines) and the theoretical profiles (full lines).

predicts a constant width for the shock but experimentally the thickness increases with time. Decreasing $Pe$ further would smooth the rapid change in concentration but the slope would still remain constant. After 23 h, the bottom of the sediment reaches a maximum packing $\phi = 0.63$. (Numerical predictions for 11, 46 and 95 h are not presented.)

These observations suggest different stresses acting on the particles at different stages of the process. An intermediate region appears, with $0.35 < \phi < 0.56$, where the settled flocs rearrange to form a new network which then consolidates. The difference between the intermediate phase and the consolidated region below it comes from the relation between the effective stress and the solids fraction. In the sediment the effective stress/solid fraction function can reasonably be expected to be unique but appears not to be so in the intermediate zone. In this deforming assembly of particles the structure is far from equilibrium so the stresses may well depend on the history of the deformation as for other non-Newtonian systems. However, adequate constitutive equations are not available.

### 6.2.2. *Numerical comparison for $d_{\mathrm{TEM}} = 0.60$ µm in cyclohexane*

Figure 13 presents the experimental values of the flux as a function of solids fractions for $d_{\mathrm{TEM}} = 0.60$ µm. The full line, calculated with equation (20), shows only one concave region. From an initial solids fraction $\phi_0 = 0.092$, direct contact between the initial suspension and the sediment surface is not possible nor can a compression shock propagate to regions which can contact the rising sediment. Hence we must construct a solution in which $\phi$ changes continuously from $\phi_0$ to the sediment concentration and the top of the suspension falls at a monotonically decreasing rate until all particles have joined the sediment.

Numerical integrations of the equation of motion at $Pe = 750$ chosen (rather than $5.5 \times 10^4$ as expected from (9)) to reproduce the smooth variation in volume fraction within the equilibrium sediment (311 h) simulate the experimental profile throughout

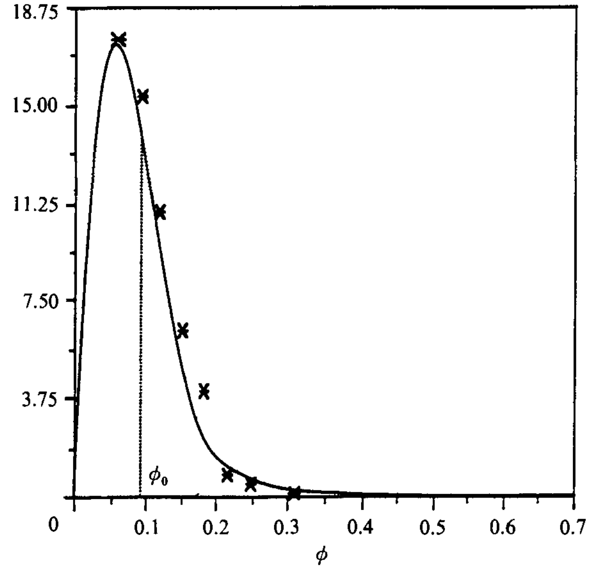

FIGURE 13. Schematic illustration of a flux curve with associated discontinuities for $d_{\text{TEM}} = 0.60\ \mu\text{m}$.

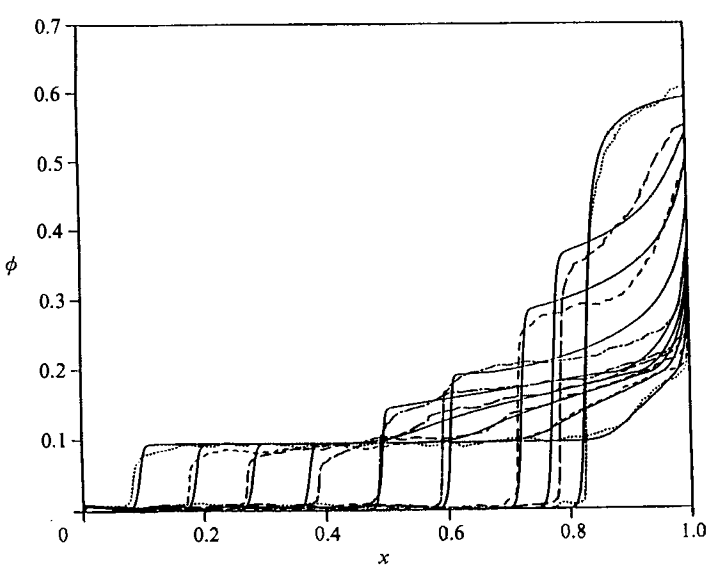

FIGURE 14. Concentration profiles at various times (10, 20, 30, 42 min; 1, 3, 23, 71, and 311 h) for $\phi_0 = 0.092$ and $Pe = 750$ for weakly flocculated suspension in cyclohexane ($d_{\text{TEM}} = 0.60\ \mu\text{m}$). Comparison between the experimental data (broken lines) and the theoretical profiles (full lines).

the suspension. Figure 14 compares the concentration profiles at 10, 20, 30, 42 min, 1 and 3 h with the theoretical results (full lines) for the same times. Concentration gradients form at the bottom of the container and propagate upward to meet the zone of initial concentration. The experimental data at 23 h and 71 h compare with theoretical plots at much shorter times (4 h and 16 h instead) but provide a qualitative appreciation of the behaviour of the system. A better representation of the phenomena would require either a refined estimate of the sedimentation velocity (20) for $\phi > 0.19$ or a more appropriate expression for the stress, accounting for significant interparticle forces throughout the sediment.

Nonetheless, experimental and theoretical results agree qualitatively. Since the duration of the settling of the individual floc is short compared with the consolidation process, the extended network gives the suspension structural properties similar to the previous example. Both samples will be discussed in §6.4.

### 6.3. *Estimation of the compressive yield stress $\sigma(\phi)$ for a strongly flocculated system from centrifuge experiments*

Centrifugal acceleration of a strongly flocculated network never totally consolidates the solid phase. Rather, the sediment attains equilibrium at long times. The dependence of this steady-state sediment volume on the centrifugal acceleration can be modelled by supposing that consolidation occurs only where the compressive stress exceeds the yield stress $\sigma(\phi)$. At steady state, $t \rightarrow \infty$, the time derivative in (4) vanishes, and the interparticle force must balance the gravitational field according to

$$U(\phi)\left[\phi - \frac{\mathrm{d}\sigma/\mathrm{d}\phi}{(\rho-\rho_f)\, g(z)\, L} \frac{\partial \phi}{\partial x}\right] = 0, \tag{21}$$

with

$$g(z) = \frac{z}{R} g \tag{22}$$

and

$$g = \omega^2 R, \tag{23}$$

with $\omega$ the angular velocity of the rotor (see figure 8). The stress at any point within the sediment then follows from integrating (21):

$$\sigma(z) = \omega^2 \, (\rho - \rho_f) \int_{R-L}^{z} x\phi(x)\, \mathrm{d}x. \tag{24}$$

Thus with the values of $\phi(x)$ from the measurements for $R-L = 60$ mm and $L = 10^2$ mm for different values of $g$ we can translate curves representing solids fraction against height, (24), into curves of interparticle stresses against solids content.

Numerical integrations of the concentration profiles for particles with $d_{\mathrm{TEM}} = 0.08\,\mu\mathrm{m}$ (figure 7), spun in the centrifuge, illustrate this method. The computed stresses plotted against solids fraction in figure 15 for a range of rotor speeds (1500 to 7000 r.p.m.) indicate three different regions, which might be fitted by power-law curves of the type

$$\sigma(\phi) = \sigma_0 \phi^n, \tag{25}$$

as for other experimental systems such as polystyrene latex (Buscall *et al.* 1988), or the divergent form (8) of the osmotic pressure. The first region, up to $\phi = 0.30$, shows an increase in $\sigma(\phi)$ proportional to $\phi^3$ with a prefactor $\sigma_0$ of about 50 kPa. In the intermediate region $0.3 < \phi < 0.5$ the stress increases faster, as $\sigma(\phi) \sim \phi^5$, and in the third region, $\phi \geqslant 0.5$, $\sigma(\phi)$ diverges as $(0.64-\phi)^{-1}$. As yet no theoretical form for $\sigma(\phi)$ has been constructed, so the physical significance of the fitting parameters remains to be determined.

The stresses falling below the bounding locus discussed above correspond to unconsolidated regions with $\sigma < \alpha(\phi_0)$. When we apply an external field to a network, the stress increases until the compressive yield stress is exceeded and the structure begins to deform irreversibly. Bonds between particles rupture, the system

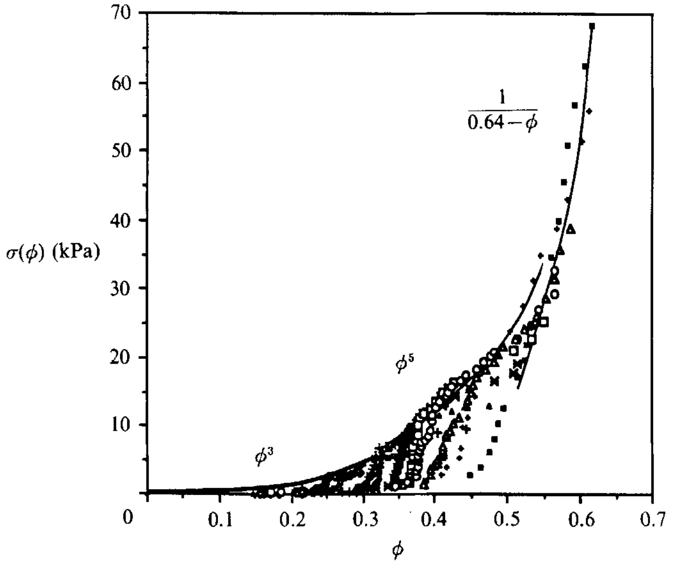

FIGURE 15. Effect of volume fraction on the interparticle stress for $d_{\text{TEM}} = 0.08$ μm in hexadecane with $\phi_0 = 0.096$ for various centrifugal accelerations (◇, 1500 r.p.m.; ■, 2000 r.p.m.; +, 2500 r.p.m.; ▲, 3000 r.p.m.; ×, 3500 r.p.m.; □, 4000 r.p.m.; ○, 4500 r.p.m.; △, 5000 r.p.m.; ◆, 6000 r.p.m.; ■, 7000 r.p.m.).

consolidates and, consequently, new and more bonds form until the network becomes strong enough to oppose the external force once more. The process apparently is not as simple as presumed in the model as the data below the locus do not fall on a single vertical asymptote as expected. Instead the consolidation appears to be history dependent.

The only results available for comparison derive from measurements of the initial rate of consolidation in similar experiments (Buscall *et al.* 1988). There, a variety of electrostatically stabilized dispersions – polystyrene latices ($2a$ = 170–960 nm), silica ($2a$ = 26 nm), and attapulgite clay (~ 100 nm × 1000 nm) – were flocculated by the addition of electrolyte; hence, van der Waals attractions bind the networks. The compressive yield stress proved a strong function of volume fraction, diameter, and composition. For example, for the latices at $\phi = 0.1$ the yield stress increased from less than $10^{-1}$ kPa to greater than 10 kPa with decreasing particle size. Generally though, these unconsolidated systems displayed much higher yield stresses in the lower range of volume fractions, $0.05 \leqslant \phi \leqslant 0.25$, than our dispersions. Given the different origin for the attraction and the possibility of a considerable different microstructure, this is not surprising.

### 6.4. *Discussion*

The settling of silica particles has been examined as a function of particle size and solvent quality. As shown in figure 9, the classical theory predicts qualitatively the transient settling behaviour of colloidally stable suspensions with the flux curve and the osmotic pressure governing the characteristics of the discontinuities/transitions and the falling rate period. However, within the sediment, numerical solutions do not resemble the experimental results since the sediment develops a crystalline or ordered structure, evidenced by an iridescent layer. de Kruif *et al.* (1985) noticed the hard-sphere phase transition for this range of particle sizes and ascribed the iridescence to the formation of small ordered domains. This phase transition produces the difference in concentrations measured between the top of the sediment ($\phi = 0.68$) and the base of the settling column ($\phi = 0.67$) (Davis *et al.* 1989).

With the appropriate flux curve, the theory predicts reasonably well the transient settling of the weakly flocculated dispersions. However, the faster settling of the smaller particles with weak London–van der Waals attractions is puzzling. To account for this apparent difference in floc sizes requires an examination of the various forces exerting an influence. In addition to dispersion forces, weakly flocculated suspensions are subjected, under settling, to viscous forces which eventually limit the floc size. If we model the floc as an impermeable sphere of radius $a_f$ consisting of small spheres at a surface-to-surface separation $h$, the viscous force on a single particle at the periphery of the floc is

$$6\pi\mu a\ v_t \frac{a}{a_f}, \tag{26}$$

where $v_t$ is the terminal velocity of the floc, and the dispersion force holding two spheres in the floc together is, from (16),

$$\frac{1}{12}\frac{A_{\text{eff}}\,a}{h^2}. \tag{27}$$

So the ratio of these two forces suggests that individual particles will add to the floc until the radius attains a maximum

$$a_f = \frac{A_{\text{eff}}}{16\pi h^2 \Delta\rho g}\frac{1}{a}, \tag{28}$$

which increases with decreasing particle radius. Our experimental results indicate the same trend as aggregates with $d_{\text{TEM}} = 0.60\ \mu\text{m}$ settle faster than with $d_{\text{TEM}} = 0.94\ \mu\text{m}$.

The flocculation of these two systems ($d_{\text{TEM}} = 0.94$ and $0.60\ \mu\text{m}$) results in a second effect, the formation of an intermediate region. For instance, between $\phi = 0.35$ and $\phi = 0.56$ (for $d_{\text{TEM}} = 0.94\ \mu\text{m}$) the suspension and sediment become difficult to differentiate. This transition zone, which covers a wide range of solids fractions, has been observed by many authors (Michaels & Bolger 1962; Tiller 1981; Been & Sills 1981; and Landman, Buscall & White 1988). The initial aggregates settle rapidly but, upon collision with other flocs, stick to create an open network at a lower average volume fraction than stable suspensions. Once the average particle volume fraction is high enough to form a network of connected particles, compressive stresses can be transmitted throughout the network and support it against the force of gravity. Further consolidation occurs as the sediment depth increases sufficiently to exceed the yield stress of the network. Inclusion of these interparticle forces in the theory might explain the disparities that emerge after about 23 h but too little is known currently to formulate appropriate constitutive equations.

Experiments with strongly flocculated dispersions show that the interparticle stresses remain important throughout the network. Centrifuge experiments seem to indicate transitions between different structures and provide a relationship between the interparticle stress and the solids fraction that is consistent with measurements of others.

## 7. Conclusion

A medical computer tomography (CT) scanner provides an accurate non-destructive method of examining the concentration or consolidation of stable and flocculated suspensions of silica particles without disrupting the process. We illustrate the performance of the scanner and provide a calibration of density or solids fraction against attenuation. The CT scanner detected the solids fraction with a relative accuracy of 2% and a spatial resolution of the order of 2 mm. In addition to detecting axial variations in the density, mapping the spatial distribution across the settling column provided information on wall effects. Also, numerous opportunities exist to improve the resolution, speed of data acquisition, and image formate for studying other processes.

We tested a theory reported previously with colloidal suspensions having narrow size distributions. Coated monodisperse silica particles permit the interactions between the particles to be varied through the nature of the solvent. With cyclohexane as a solvent, submicron particles behave as hard spheres, but hexadecane induces flocculation. The magnitude of the dispersion energy for larger particles in cyclohexane indicates weakly flocculated suspensions. With hard-sphere particles, the transition from the uniform suspension at $\phi = 0.10$ to the falling rate region at $\phi = 0.42$ appears as predicted and the intermediate concentrations closely resemble those computed. For weakly flocculated silica dispersions in cyclohexane the kinetics of sedimentation within the dispersed phase follows from the flux curve. With an initial solids fraction of $\phi_0 = 0.12$ for silica particles of 0.94 μm diameter, the double concavity in the flux curve induces intermediate shocks between two regions of continuously varying concentration. But comparing the short duration of the settling of the individual floc with the long consolidation process suggests a time-dependent rearrangement from an open network to one comprising a more condensed collection of clusters. A natural extension of our experimental work would be to investigate the dynamics of this intermediate region.

For flocculated networks consolidated in a centrifuge, horizontal concentration profiles indicate a greater concentration at the wall than at the centre of the tube, due to radial variations in the field. However, the relationship between compressive yield stresses and solids fractions conforms reasonably well with other experimental systems such as polystyrene latex (Buscall 1990) and demonstrates an important feature of flocculated networks. Even though the theory described for the settling of flocculated materials is a meaningful first step, other factors obviously must be included to complete the treatment.

We wish to acknowledge support for this work from the National Science Foundation's Fluid, Particulate and Hydraulic Systems Program, under grant No. CBT-8504201, the Petroleum Research Fund, and the Westvaco Foundation.

## REFERENCES

AUZERAIS, F. M., JACKSON, R. & RUSSEL, W. B. 1988 The resolution of shocks and the effects of compressible sediments in transient settling. *J. Fluid Mech.* **195**, 437–462.

BARCLAY, L., HARRINGTON, A. & OTTEWILL, R. H. 1972 The measurement of forces between particles in disperse systems. *Kolloid-Z.-u.Z. Polymere* **250**, 655–666.

BATCHELOR, G. K. 1972 Sedimentation in a dilute dispersion of spheres. *J. Fluid Mech.* **52**, 245–268.

BATCHELOR, G. K. 1976 Brownian diffusion of particles with hydrodynamic interactions. *J. Fluid Mech.* **74**, 1–29.

BEEN, K. & SILLS, G. C. 1981 Self weight consolidation of soft soils: an experimental and theoretical study. *Geotechnique* **31**, 519–535.

BOGUSH, G. H. & ZUKOSKI, C. F. 1986 The colloidal chemistry of growing silica spheres. *Proc. Microstructures, Berkeley, Ca., July.*

BUSCALL, R. 1981 The elastic properties of structured dispersions: a simple centrifuge method of examination. *Colloids Surf.* **5**, 269–283.

BUSCALL, R. 1990 The sedimentation of concentrated colloidal suspensions. *Colloids Surf.* **43**, 33–53.

BUSCALL, R., GOODWIN, J. W., OTTEWILL, R. H. & TADROS, TH. F. 1982 The settling of particles through newtonian and non-newtonian media. *J. Colloid Interface Sci.* **85**, 78–86.

BUSCALL, R., MILLS, P. D. A., GOODWIN, J. W. & LAWSON, D. W. 1988 Scaling behaviour of the rheology of aggregate networks formed from colloidal particles. *J. Chem. Soc. Faraday Trans.* I **84**, 4249–4260.

BUSCALL, R. & WHITE, L. R. 1987 The consolidation of concentrated suspensions. *J. Chem. Soc. Faraday Trans.* I **83**, 873–891.

CARSLAW, H. S. & JAEGER, J. C. 1959 *Conduction of Heat in Solids*, p. 206. Oxford University Press.

DAVIS, K. E. & RUSSEL, W. B. 1989 An asymptotic description of transient settling and ultrafiltration of colloidal dispersions. *Phys. Fluids* A **1**, 82–100.

DAVIS, K. E., RUSSEL, W. B. & GLANTSCHNIG, W. J. 1989 Disorder-to-order transition in settling suspensions of colloidal silica: X-ray measurements. *Science* **245**, 507–510.

DERJAGUIN, B. V. & LANDAU, L. D. 1941 Theory of the stability of strongly charged lyophobic sols and the adhesion of strongly charged particles in solutions of electrolytes. *Acta Physicochim. URSS* **14**, 633–662.

FITCH, B. 1986 In *Solid/Liquid separation scale-up, clarification and thickening*, Chap. 4. (ed. D. B. Purhcas & R. J. Wakeman) London: Uplands.

GAUDIN, A. M. & FUERSTENAU, M. C. 1958 *Eng. Mining J.* **159**, 110.

HOUNSFIELD, G. N. 1972 A method of and apparatus for examination of a body by radiation such as X- or Gamma-radiation. British patent No 1,283,915, London.

HOWE, A. M. & ROBINS, M. M. 1990 Determination of gravitational separation in dispersions from concentration profiles. *Colloids Surf.* **43**, 83–94.

JANSEN, J. W., KRUIF, C. C. DE & VRIJ, A. 1986*a* Attractions in sterically stabilized silica dispersions. II. Experiments on phase separation induced by temperature variation. *J. Colloid Interface Sci.* **114**, 481–491.

JANSEN, J. W., KRUIF, C. G. DE & VRIJ, A. 1986*b* Attractions in sterically stabilized silica dispersions. IV. Sedimentation. *J. Colloid, Interface Sci.* **114**, 481–491.

KOPS-WERKHOVEN, M. M. & FIJNAUT, H. M. 1981 Dynamic light scattering and sedimentation experiments on silica dispersions at finite concentration. *J. Chem. Phys.* **74**, 1618–1625.

KRUIF, C. G. DE, JANSEN, J. W. & VRIF, A. 1987 A sterically stabilized silica colloid as a model supramolecular fluid. In *Physics of Complex and Supramolecular Fluids*, pp. 315–347. Wiley Interscience.

KRUIF, C. G. DE, ROUW, P. W., JANSEN, J. W. & VRIJ, A. 1985 Hard sphere properties and crystalline packing of lyophilic silica colloids. *J. Phys. Colloq.* C3 **46**, 295–308.

KYNCH, G. J. 1952 A theory of sedimentation. *Trans. Faraday Soc.* **48**, 166–176.

LANDMAN, K. A., BUSCALL, R. & WHITE, L. R. 1988 The continuous flow gravity thickener: steady state behaviour. *AIChE J.* **34**, 239–252.

MAHANTY, J. & NINHAM, B. W. 1976 *Dispersion Forces*. Academic.

MATIJEVIC, E. 1976 Preparation and characterization of monodisperse metal hydrous oxide sols. *Prog. Colloid Polymer Sci.* **61**, 24–35.

MICHAELS, A. A. & BOLGER, J. C. 1962 Settling rates and sediment volumes of flocculated kaolin suspensions. *Ind. Engng Chem. Fundam.* **1**, 24–33.

ONDEKA, J. G., HENRY, J. D. & VERHOFF, F. H. 1978 Indirect measurement of sedimentation rates at high temperature and pressure by X-ray photography. *Ind. Engng Chem. Fundam.* **3**, 217–221.

OTTEWILL, R. H. 1980 Direct measurements of particle-particle interactions. *Prog. Colloid Polymer Sci.* **67**, 71–83.

PAYNE, J. T. & MCCULLOUGH, E. C. 1976 Basic principles of computer-assisted tomography. *Appl. Radiol.* March-April, pp. 230–39.

RHEE, H. K., ARIS, R. & AMUNDSON, N. R. 1976 *First order Partial Differential Equations. Vol I, Theory and Application of Single Equations*, pp. 350–360. Prentice-Hall.

ROSCOE, K. H., ARTHUR, J. R. F. & JAMES, R. G. 1963 Strains in soils by X-ray method. *Civil Engng Public Works Rev.* July, 873–1012.

RUSSEL, W. B., SCHOWALTER, W. R. & SAVILLE, D. A. 1989 *Colloidal Dispersions*. Cambridge University Press.

SHANNON, P. T., DEHAAS, R. D., STROUPE, E. P. & TORY, E. M. 1964 Batch and continuous thickening. *Ind. Engng Chem. Fundam.* **3**, 250–260.

SHANNON, P. T., STROUPE, E. P. & TORY, E. M. 1963 *Ind. Engng Chem. Fundam.* **2**, 203.

STÖBER, W., FINK, A. & BOHN, E. 1968 Controlled growth of monodisperse silica spheres in the micron size range. *J. Colloid Interface Sci.* **26**, 62–69.

TAN, C. G., BOWEN, B. D. & EPSTEIN, N. 1967 Production of monodispersed colloidal silica spheres: effect of temperature. *J. Colloid Interface Sci.* **118**, 290–293.

THIELE, E. 1963 Equation of state for hard spheres. *J. Chem. Phys.* **39**, 474–477.

TILLER, F. M. 1981 Revision of Kynch sedimentation theory. *AIChE J.* **27**, 823–829.

TILLER, F. M. & YEH, C. S. 1990 Relative liquid removal in filtration and expression. *Filtr. Sep.* **27**, 123–135.

TORY, E. M. 1961 Batch and continuous thickening of slurries. Ph.D. thesis, Purdue University.

VAN HELDEN, A. K., JANSEN, J. W. & VRIJ, A. 1981 Preparation and characterization of spherical monodisperse silica dispersions in nonaqueous solvents. *J. Colloid Interface Sci.* **81**, 354–368.

VERWEY, E. J. W. & OVERBEEK, J. TH. 1948 *Theory of the Stability of Lyophobic Colloids*. Elsevier.

WELLINGTON, S. L. & VINEGAR, H. J. 1987 X-ray computerized tomography. *J. Petrol. Techn.* August, 885–898.

WOODCOCK, L. V. 1981 Glass transition in the hard-sphere model and Kauzmann's paradox. *Ann. NY Acad. Sci.* **37**, 274–298.